

Metal–Ligand Covalency of Iron Complexes from High-Resolution Resonant Inelastic X-ray Scattering

Marcus Lundberg,^{†,||} Thomas Kroll,[†] Serena DeBeer,^{‡,⊥} Uwe Bergmann,[‡] Samuel A. Wilson,[†] Pieter Glatzel,[§] Dennis Nordlund,[‡] Britt Hedman,^{*,‡} Keith O. Hodgson,^{*,†,‡} and Edward I. Solomon^{*,†,‡}

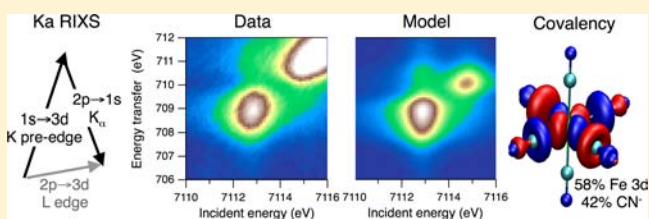
[†]Department of Chemistry, Stanford University, Stanford, California 94305, United States

[‡]Stanford Synchrotron Radiation Lightsource, SLAC National Accelerator Laboratory, Stanford University, Menlo Park, California 94025, United States

[§]ESRF, BP 220, 38043 Grenoble, Cedex 9, France

Supporting Information

ABSTRACT: Data from $K\alpha$ resonant inelastic X-ray scattering (RIXS) have been used to extract electronic structure information, i.e., the covalency of metal–ligand bonds, for four iron complexes using an experimentally based theoretical model. $K\alpha$ RIXS involves resonant $1s \rightarrow 3d$ excitation and detection of the $2p \rightarrow 1s$ ($K\alpha$) emission. This two-photon process reaches similar final states as single-photon L-edge ($2p \rightarrow 3d$) X-ray absorption spectroscopy (XAS), but involves only hard X-rays and can therefore be used to get high-resolution L-edge-like spectra for metal proteins, solution catalysts and their intermediates. To analyze the information content of $K\alpha$ RIXS spectra, data have been collected for four characteristic σ -donor and π -back-donation complexes: ferrous tacn [$\text{Fe}^{\text{II}}(\text{tacn})_2$] Br_2 , ferrocyanide [$\text{Fe}^{\text{II}}(\text{CN})_6$] K_4 , ferric tacn [$\text{Fe}^{\text{III}}(\text{tacn})_2$] Br_3 and ferricyanide [$\text{Fe}^{\text{III}}(\text{CN})_6$] K_3 . From these spectra metal–ligand covalencies can be extracted using a charge-transfer multiplet model, without previous information from the L-edge XAS experiment. A direct comparison of L-edge XAS and $K\alpha$ RIXS spectra show that the latter reaches additional final states, e.g., when exciting into the e_g (σ^*) orbitals, and the splitting between final states of different symmetry provides an extra dimension that makes $K\alpha$ RIXS a more sensitive probe of σ -bonding. Another key difference between L-edge XAS and $K\alpha$ RIXS is the π -back-bonding features in ferro- and ferricyanide that are significantly more intense in L-edge XAS compared to $K\alpha$ RIXS. This shows that two methods are complementary in assigning electronic structure. The $K\alpha$ RIXS approach can thus be used as a stand-alone method, in combination with L-edge XAS for strongly covalent systems that are difficult to probe by UV/vis spectroscopy, or as an extension to conventional absorption spectroscopy for a wide range of transition metal enzymes and catalysts.



1. INTRODUCTION

First-row transition metals form the active site of many homogeneous, heterogeneous and biological catalysts. The ability of metalloenzymes to accelerate and control even the most complicated chemical processes makes them important, both in biochemistry and as inspirations for new synthetic catalysts. Development of better catalysts requires knowledge about electronic structure of the metal 3d orbitals involved in metal–ligand bonding and catalysis. X-ray spectroscopy involving a core-hole offers a unique local and element-specific probe, but the challenges for biological and solution systems have been to: (a) obtain spectra with sufficiently high energy resolution so that the main electronic transitions can be observed, and (b) to extract detailed electronic structure information from the X-ray spectra. Progress in instrumentation and the use of resonant inelastic X-ray scattering (RIXS) to limit the lifetime broadening shows that the first challenge can be overcome.^{1,2} The purpose of the present study is to show how hard X-ray RIXS can be used to extract the metal–ligand covalency of the 3d orbitals in transition metal systems. The

method can potentially become a standard tool to analyze the relationship between electronic structure and catalytic activity for a wide range of enzymes and catalytic systems.

Transition metal complexes are intensively studied by UV/vis spectroscopy, but the specificity to the catalytic metal is lost if groups other than the metal absorb strongly in the same region. L-edge ($2p \rightarrow 3d$) X-ray absorption (XAS) is an element-specific technique, rich in information about the reactive 3d orbitals. However, due to strong absorption of soft X-rays from the sample environment, it cannot be directly used for enzymes and solution catalysts. The standard X-ray probes of transition metal catalysts in biological and solution systems use hard X-rays (4–10 keV), either metal K-edge XAS or $K\alpha/K\beta$ X-ray emission spectroscopy (XES),¹ because high-energy X-ray photons are only weakly absorbed by the sample environment. In metal K-edge XAS the pre-edge ($1s \rightarrow 3d$ excitations) gives information about oxidation state and the

Received: August 8, 2013

Published: October 16, 2013

symmetry of the ligand environment,^{3–5} but is less sensitive to the electronic structure of the 3d orbitals. In addition, the short lifetime of the 1s hole in the final state leads to a large lifetime broadening (1–2 eV), which obscures spectral detail. $K\beta$ valence XES gives information about the identity of the metal ligands,^{6,7} but this spectral region is dominated by electric dipole allowed transitions from valence orbitals with metal 4p character. The quadrupole allowed 3d \rightarrow 1s transitions show up as weak features on the higher energy side of the valence-to-core XES, and spectral resolution is again obscured by the short lifetime of the 1s core hole.

During the latest decade, RIXS has emerged as a powerful tool to obtain high-resolution X-ray spectra of transition metal systems. RIXS is a two-photon process, where the energy of the incident photon (Ω) is tuned into an absorption resonance, followed by emission of a scattered photon of typically a lower energy (ω).^{8,9} This scattering process can be viewed as the X-ray analogue to resonance Raman spectroscopy. The energy difference between incident and emitted photons, i.e., the energy transfer ($\Omega-\omega$), corresponds to the energy of the fundamental process that is probed, e.g., a core, valence or charge-transfer excitation.^{10–13} An important advantage of RIXS is that the lifetime broadening in the energy transfer direction only depends on the lifetime of the final state, not the lifetime of the short-lived core hole in the intermediate state.^{14–17} This makes it possible to achieve high-resolution energy transfer spectra while still keeping the advantages of the X-ray probe.^{2,18–20}

To probe the 3d orbitals of low-concentration samples that can be subject to rapid degradation in the X-ray beam, the preferred scattering process is 1s \rightarrow 3d excitation followed by detection of the strongest emission channel, the $K\alpha$ (2p \rightarrow 1s) emission, see Figure 1. This method is labeled $K\alpha$ RIXS,

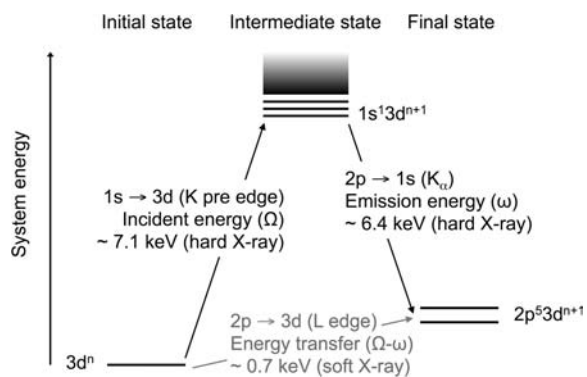


Figure 1. Two-step total energy schematic of the $K\alpha$ RIXS process. The vertical axis shows the total energy of the electron configuration. Photon energies are shown for the case of an iron complex.

referring to the emission line, or 1s2p RIXS, referring to the 1s hole in the intermediate state and the 2p hole in the final state. $K\alpha$ RIXS data have already been collected for several enzymes and solution catalysts e.g., photosystem II²¹ and Ni–Fe hydrogenase,¹ as well as hydrogenase mimics.²²

The final state in the $K\alpha$ RIXS process has an orbital occupation of $2p^5 3d^{n+1}$, where n is the number of 3d electrons in the ground state. This is the same final-state configuration as in the single-photon L-edge (2p \rightarrow 3d) excitation. The energy transfer in the $K\alpha$ RIXS experiment thus corresponds to the direct L-edge absorption energy, and the resolution is limited by the lifetime of the 2p core hole in the final state. Projections

along the energy transfer axis in $K\alpha$ RIXS thus makes it possible to obtain L-edge-like spectra^{1,23,24} for samples where direct XAS in the soft X-ray regime have inherent experimental difficulties, such as enzymes and solution catalysts.²⁵ However, to take advantage of the high resolution of the RIXS experiment requires a special experimental setup. Although research on low-energy excitations in magnetic materials and superconductors^{26,27} has achieved a resolution at below 0.1 eV for hard X-rays,^{2,20} in many chemistry applications it is more important to get higher detection efficiency at more moderate resolutions. In the present study the target is an instrument resolution close to the lifetime broadening of the iron L_3 edge (0.4 eV).²⁸

The line shape of the iron L-edge has previously been analyzed using a valence-bond configuration interaction (VBCI) multiplet model^{29,30} to extract the individual covalencies of the metal d-orbitals involved in σ and π donor and π acceptor bonding, i.e., the differential orbital covalency (DOC).^{31–35} However, the single-photon XAS experiment and the two-photon RIXS experiment are governed by different selection rules and intensity mechanisms.³⁶ To analyze how these differences affect the information content of the $K\alpha$ RIXS experiment and the ability to extract reliable metal–ligand covalencies, we have collected RIXS data on four low-spin iron complexes for which both the L-edge and the K-edge XAS spectra have been previously analyzed: ferrous tacn $[\text{Fe}^{\text{II}}(\text{tacn})_2]\text{Br}_2$,³¹ (tacn = 1,4,7 triazacyclononane), ferrocyanide $\text{K}_4[\text{Fe}^{\text{II}}(\text{CN})_6]$,³² ferric tacn $[\text{Fe}^{\text{III}}(\text{tacn})_2]\text{Br}_3$,³¹ and ferricyanide $\text{K}_3[\text{Fe}^{\text{III}}(\text{CN})_6]$ ³² see Figure S1 in the Supporting Information (SI). The electronic structures of these complexes are well-established: ferrous and ferric tacn are dominantly σ -donor complexes, while ferro- and ferricyanide are prototypical π -back-donation complexes.³⁷ These complexes are therefore excellent benchmarks for a method to extract metal–ligand covalencies from $K\alpha$ RIXS data.

RIXS processes have previously been modeled using a number of methods.^{15,24,38–42} The shape of the $K\alpha$ RIXS spectrum depends on a number of factors, e.g., the interactions between the 2p hole and the 3d electrons, the 3d–3d electron interactions, as well as the 2p and 3d spin–orbit coupling. The VBCI multiplet model includes all these effects at a limited computational cost,²⁹ but requires the fitting of a number of parameters to a single spectrum. In this study the differences in selection rules and intensity mechanisms between L-edge XAS and $K\alpha$ RIXS have been explained with parameters from a previous L-edge XAS study^{31,32} without changing their values when modeling the RIXS data. The fact that the VBCI multiplet model can reproduce both experiments using the same parameters supports the general validity of the model for these processes.

Hard X-ray RIXS has previously been used to study transition-metal pre-edges for a number of different materials,⁴³ using both $K\alpha$ ^{23,44,45} and $K\beta$ X-ray emission,^{46–49} What is novel in the present study is the combination of a high energy-resolution experimental setup that resolves the main electronic transition, with a theoretical model that uses the shape of the $K\alpha$ RIXS spectrum to extract the structure of orbitals involved in metal–ligand bonding. This approach thus overcomes the challenge of obtaining detailed electronic structure information about the reactive 3d orbitals using hard X-rays. This is critical for metal enzymes and other catalysts that are difficult to probe by UV/vis light, but with the increasing availability of high-brilliance X-ray sources, it can also be used as an extension to

conventional absorption spectroscopy for a wide range of transition metal enzymes and catalysts.

2. MATERIALS AND METHODS

2.1. Experimental Section. Beamline Setup for RIXS. $K\alpha$ RIXS experiments were performed at the Stanford Synchrotron Radiation Lightsource (SSRL) beamline 6-2 and at the European Synchrotron Radiation Facility (ESRF) ID 26. Each complex was measured multiple times, but to facilitate the direct comparison between complexes, the data sets presented in the present contribution are measured at ESRF ID26 using the same experimental setup. To obtain high energy resolution of the incoming radiation (~ 0.18 eV at 7 keV), the energy was monochromatized using a Si(3,1,1) double-crystal monochromator. The beam size on the sample was approximately 0.5 mm \times 0.15 mm full-width half-maximum (fwhm) with an incident flux of $\sim 10^{13}$ photons/s. The focused beam improves the resolution in the Bragg crystal spectrometer used to monochromatize the X-ray emission, but prolonged exposure to the focused beam can lead to significant sample photodamage. To limit this effect, samples were kept in a liquid helium-cooled cryostat (~ 10 K) and surrounded by an exchange gas (He). Suitable exposure times were evaluated by monitoring changes to the spectral shape during repeated scans of the pre-edge region, see the SI for more details. The RIXS plane data were measured as a series of scans, each on a different spot on the sample, with an exposure time below the limit for significant photodamage.

The X-ray emission was monochromatized using the (4,4,0) Bragg reflection of up to four spherically bent Ge analyzer crystals (100 mm diameter, 1000 mm radius of curvature) arranged in a Rowland geometry, with both the sample and the detector positioned on the Rowland circle.¹ All data presented here were collected with a mask covering the periphery of the crystals, which gives scattering from the inner 50 mm of the crystal, corresponding to a solid angle of 7.8 msr. An avalanche photodiode was used at ESRF ID26 while a solid-state Si drift detector with a 200-eV electronic window was used at SSRL BL6-2. To minimize signal attenuation in the spectrometer the entire emitted beam path was enclosed in a He-filled bag. The count rate at the RIXS pre-edge was ~ 4000 counts/s, the exposure time for each sample spot ≤ 20 s, and the data collection time for a single RIXS plane approximately 3 h.

Details of the energy calibration and intensity normalization are given in the SI.

Energy Resolution. To show that $K\alpha$ RIXS energy transfer spectra can be obtained with a resolution close to that of the equivalent L-edge XAS experiment, the width of the emission from the first core resonance in ferricyanide was measured because this final state is not split by any multiplet effects.³² When using a single-crystal monochromator, a fwhm of 0.66 eV was obtained, similar to the width of the same resonance in the L-edge XAS L_3 edge (0.62 eV) and only a minor increase compared to the natural line width (0.4 eV). This translates to a total instrumentation broadening of 0.4 eV. The data in the present paper were measured using four analyzer crystals, which improves the total signal for low-concentration samples like metalloproteins. However, as not all crystals have the same low bandwidth, this setup gave a slightly larger line width of the first resonance in ferricyanide, 0.83 eV fwhm, 0.2 eV larger than for the L-edge XAS spectrum.

K- and L-Edges. L-edge data were measured as described in reference 32, and K-edge data as described in reference 4. Fitting of K pre-edge features was performed using the EDG_FIT module of the EXAFSPAK suite⁵⁰ using pseudo-Voigt line shapes with a fixed 50:50 ratio of Lorentzian to Gaussian functions where the energy positions, the fwhm and the peak heights were varied.

Sample Preparation. $K_4[Fe^{II}(CN)_6]$ (ferrocyanide) and $K_3[Fe^{III}(CN)_6]$ (ferricyanide) were obtained from Sigma Aldrich at the highest purity available, while $[Fe^{III}(tacn)_2]Br_3$ (ferric tacn) and $[Fe^{II}(tacn)_2]Br_2$ (ferrous tacn) were synthesized according to literature methods.⁵¹ All measurements were done on powder samples, representative of the isotropy in protein and solution catalyst samples. Samples were made optically thin by diluting the pure sample with

boron nitride to 1.0 wt % of iron. The mixed samples were manually pressed into the sample holder and held in place by 25 μ m thin Kapton tape. The air-sensitive ferrous tacn sample was prepared in a glovebox and transferred to the beamline under liquid nitrogen. Despite careful packing of the sample holder, the samples were not perfectly uniform, and the emission intensity depends on the concentration in the spot where that spectrum is collected. This sample inhomogeneity was corrected by normalization at each spot to the nonresonant fluorescence signal, using an incident energy of 7150 eV.

2.2. Modeling. VBCI Multiplet Calculations. The RIXS process is an inelastic scattering of the incident photon at the Fe atom.^{8,9,13,52} At a core resonance, the cross section is totally dominated by the resonant contribution to the scattering, leading to the following form of the Kramers–Heisenberg formula:^{8,15,53,54}

$$F(\Omega, \omega) = \sum_f \left| \sum_i \left(\frac{\langle f|T_e|li\rangle \langle i|T_a|g\rangle}{E_g - E_i + \Omega - i\Gamma_i/2} \right) \right|^2 \times \delta(E_g - E_f + \Omega + \omega) \quad (1)$$

where $|g\rangle$, $|i\rangle$ and $|f\rangle$ are ground, intermediate, and final states, E_g , E_i , E_f their respective energies, Γ_i the lifetime broadenings for intermediate states that apply in the incident energy (Ω) direction, while T_a and T_e are the absorption and emission operators. Here, the delta function should be replaced by a suitable function that describes lifetime and experimental broadening in the energy transfer ($\Omega - \omega$) directions. A discussion of the treatment of lifetime and instrumental broadenings can be found in references 55–57. The limited core hole lifetime gives rise to a Lorentzian shape, while the experimental broadening depends on the spectrometer setup, and may deviate significantly from a Gaussian distribution. This makes it difficult to find an accurate analytical model for the spectral shape, and thus for simplicity the transitions were broadened using Gaussian line profiles. In the incident energy direction the lifetime broadening of the 1s hole was set to 1.2 eV (fwhm)²⁸ with an instrumental broadening of 0.3 eV. In the energy transfer direction the corresponding values were 0.4 and 0.5 eV, respectively. The broadenings have been chosen to match the width of the first resonance in the experimental ferricyanide $K\alpha$ RIXS plane.

Energies and transition matrix elements were calculated using a VBCI multiplet model, implemented in the program TT-multiplets,^{29,30} the same method as previously used to analyze the L-edge XAS spectra of the four complexes in the present study.^{31,32} K-edge absorption and emission can, due to the symmetric overlap between the 1s hole and the valence electrons, successfully be described with the use of a variety of methods,^{58,59} but in the final state of L-edge XAS and $K\alpha$ RIXS the 2p–3d and 3d–3d electron interactions, together with the spin–orbit coupling leads to complicated multiplet structures. The VBCI model includes an atomic description of electron–electron interaction and spin–orbit coupling,^{60–65} and the ligand interaction is described with the use of a ligand field⁶⁶ in the appropriate symmetry.⁶⁷ Covalent mixing of the metal d orbitals with the ligand valence orbitals is treated as a configuration interaction between a main atomic configuration and a ligand-to-metal charge transfer (LMCT) configuration that describes σ and π -donation and a metal-to-ligand charge transfer (MLCT) configuration to describe back-donation.^{29,32,68} The models for ferrous and ferric tacn include the LMCT configuration while the models for ferro- and ferricyanide also include the MLCT configuration. A three-configuration model has previously been used to model RIXS but only with two LMCT configurations.⁴¹ Thus, until this study, the understanding of the effects of MLCT on RIXS data were limited.

Starting parameters were taken from previous fits to the L-edge XAS.³² As the core-hole potential in Fe_2O_3 was estimated to be similar for 1s and 2p holes,⁴⁴ the same VBCI parameters were used for intermediate and final states. More details of the VBCI modeling are given in the SI and complete lists of parameters for L-edge XAS and $K\alpha$ RIXS modeling are given in Tables S1 and S2 in SI. To be consistent with previous L-edge modeling, O_h symmetry was used for all systems. Effects of deviations from that symmetry, e.g., from the

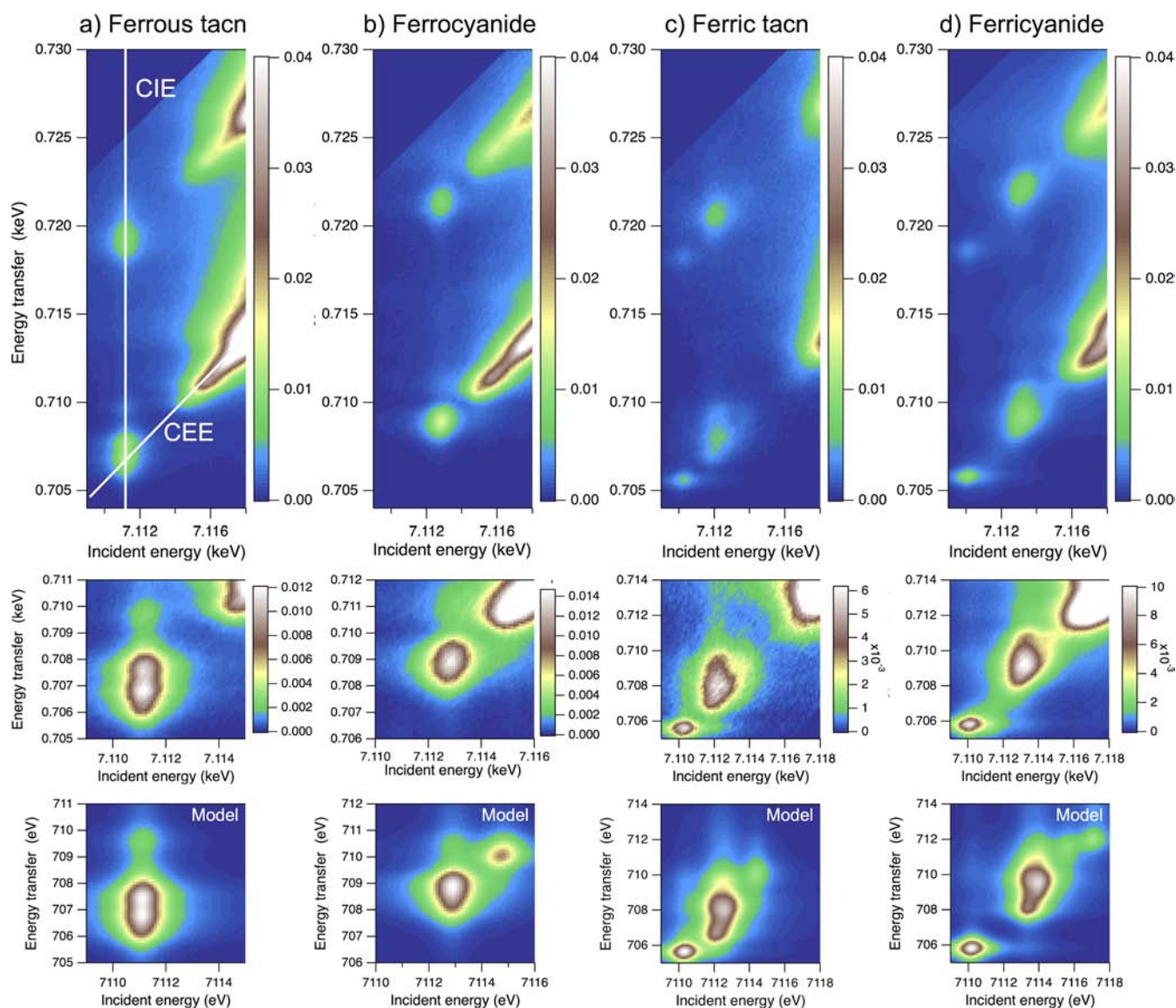


Figure 2. Experimental RIXS planes for ferrous tacn $[\text{Fe}^{\text{II}}(\text{tacn})_2]\text{Br}_2$, ferrocyanide $[\text{Fe}^{\text{II}}(\text{CN})_6]\text{K}_4$, ferric tacn $[\text{Fe}^{\text{III}}(\text{tacn})_2]\text{Br}_3$ and ferricyanide $[\text{Fe}^{\text{III}}(\text{CN})_6]\text{K}_3$ (first row). In the ferrous tacn spectrum, white lines show constant incident energy (CIE) and constant emission energy (CEE) cuts. The second row shows expanded pre-edge regions where the maximum of the color scale corresponds to the peak of the pre-edge. The third row shows VBCI modeling results for the corresponding pre-edge region. As the model only includes quadrupole transitions, the dipole-dominated rising edge is not described. Full RIXS spectra from the VBCI model are shown in Figure S2 in SI.

Jahn–Teller distortion in ferric complexes, were considered as described in the SI.

The total amplitude $F(\Omega, \omega)$ in eq 1 was calculated as the product of the squared amplitude of absorption and emission matrix elements. This two-step approximation neglects potential interference between final states originating from different intermediate states.^{8,39,72} In centrosymmetric complexes the main contribution to the K pre-edge is from the electric quadrupole operator.^{3,69,70} Dipole contributions from vibrational coupling have been estimated to be negligible for ferrocyanide and less than 5% for ferricyanide.⁷¹ The matrix elements for the K pre-edge absorption were therefore calculated using the quadrupole operator, while the $2p \rightarrow 1s$ emission is calculated using the dipole operator. However, the approach is not restricted to centrosymmetric systems. For other systems, contributions from electric dipole-allowed transitions into molecular orbitals with metal 4p character can be included in the multiplet model using an additional 3d-to-4p charge transfer configuration.

When calculating the differential orbital covalency using L-edge XAS, the integrated spectral intensity was used to estimate the total

amount of metal 3d character in the unoccupied valence orbitals, and to calibrate the calculated total covalency.³¹ However, in the RIXS experiment the sensitivity to other factors, such as exact experimental geometry, rendered this normalization unstable and the integrated pre-edge intensity varied by up to 20% between different beam times. This variability made it difficult to calculate accurate experimental covalencies from the present RIXS data. To facilitate the comparison with the previous L-edge XAS analysis, values for the total covalency were taken from the L-edge study.³² For other systems, an accurate total covalency correction requires either a more stable intensity calibration, or data from other experiments, e.g., the metal K pre-edge.

Density Functional Calculations. Density-functional modeling was performed to obtain geometries and estimates of metal and ligand contributions to the molecular orbitals. Calculations were performed using Gaussian09,⁷³ with population analysis done using QMForge.⁷⁴ To test the stability of the results, calculations were done with both BP86 and B3LYP functionals, and using the 6-31G(d) and 6-311+G(2df,2pd) basis sets. The compositions of the virtual orbitals are not well-defined in ground state DFT calculations due to the fact that

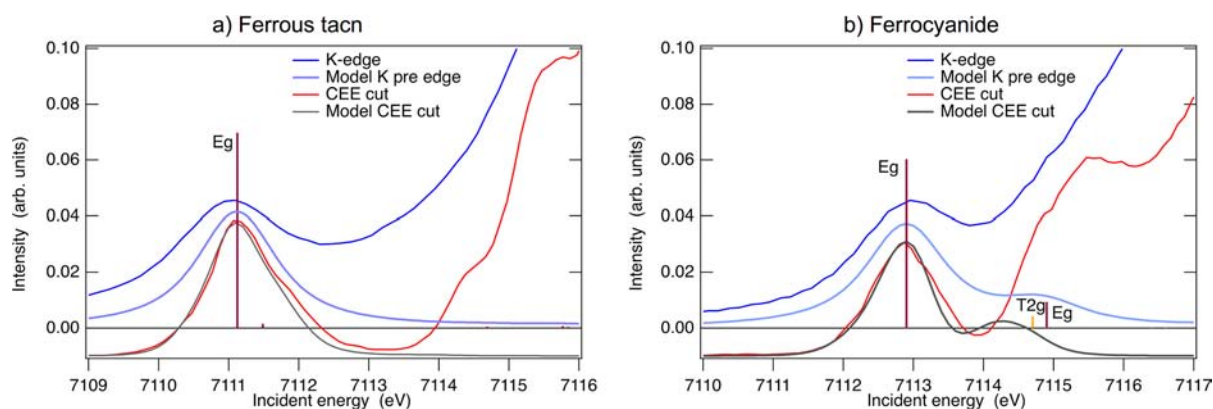


Figure 3. Spectra in the K pre-edge region for ferrous tacn (left) and ferrocyanide (right). Experimental K pre-edge spectra (blue) are compared to the spectra from the VBCI multiplet model (light blue). Modeled absorption resonances are shown as sticks. Experimental CEE cuts through the maximum of the pre-edge resonance (red) are compared to the corresponding cuts through the modeled RIXS plane (gray). The CEE cuts are arbitrarily scaled to facilitate comparison with the K pre-edge.

the electron density, and thus the total energy, only depends on the occupied orbitals. However, in many cases the composition of the virtual orbitals are correlated to the composition of the corresponding occupied orbitals, and we assume that the population analysis gives reasonable insights into the composition of the virtual orbitals.

3. RESULTS AND ANALYSIS

The $K\alpha$ RIXS spectra of all four complexes are shown in Figure 2. The data are plotted in a two-dimensional representation with the two axes being the incident energy (Ω) and the energy transfer ($\Omega - \omega$).^{15,23,43} All planes have two regions with high intensity, stretching roughly diagonally across the plane. The region at lower energy transfer values is the $K\alpha_1$ emission with final states corresponding to the L_3 ($J = 3/2$) edge of the L-edge XAS, and the upper region is the $K\alpha_2$ emission, which corresponds to the L_2 ($J = 1/2$) edge. The splitting of approximately 12 eV is due to the 2p spin-orbit coupling in the final state. Each resonance has lifetime broadening in the incident energy direction that comes from the limited lifetime of the 1s hole (~ 1.2 eV), and a lifetime broadening in the energy transfer direction from the limited lifetime of the 2p hole (~ 0.4 eV for L_3 and ~ 0.8 eV for L_2).¹

The two-dimensional RIXS spectrum probes d-d interactions and 3d spin-orbit coupling along the incident energy axis, while the energy transfer axis probes the 2p-3d interactions and the 2p spin-orbit coupling. This is a principal advantage compared to L-edge XAS where all interactions appear along the same energy axis, but the higher dimensionality of RIXS makes it more difficult to visualize spectral details. To facilitate the analysis, a number of cuts can be made through the RIXS plane. Cuts along constant emission energy (CEE), i.e., diagonally through the plane, see Figure 2a, give the high energy-resolution fluorescence detected (HERFD) X-ray absorption near-edge spectrum (XANES).^{14,18,55,75,76} Cuts at constant incident energy (CIE), see Figure 2a, take full advantage of the high resolution in the energy transfer direction and generate “L-edge-like” energy transfer spectra.^{1,23,24} An alternative is to integrate the CIE spectra along the incident energy. These spectra include contributions from all $2p^5 3d^{n+1}$ final states reached in the RIXS process, which facilitates the direct comparisons between RIXS and L-edge XAS.

3.1. RIXS Spectrum of Ferrous tacn. Ferrous tacn is a low-spin ferrous complex (d^6), with six coordinating nitrogen

atoms at equal distance, see Figure S1 in SI. It has formal D_3 symmetry, with N-Fe-N angles between 83° and 97° , but can at a first approximation be modeled using O_h symmetry. The ground state is fully symmetric because the six d-electrons fill the t_{2g} shell while the e_g shell is empty, see Figure S3 in SI. The t_{2g} shell is essentially nonbonding while the e_g orbitals are antibonding (σ^*) metal-ligand orbitals that describe σ -donation.

As described above, the ferrous tacn $K\alpha$ RIXS spectrum has two high-intensity regions, separated by the 2p spin-orbit coupling in the final state, see Figure 2a. Both regions have a K pre-edge absorption resonance centered at an incident energy of 7111.1 eV, well separated from the rising edge. The pre-edge peak is shaped like a figure eight with two separate maxima, at 706.8 and 707.6 eV energy transfer for the L_3 edge, see Figure 2a. At the same incident energy there is also a very weak resonance at 709.7 eV.

Incident Energy Direction. A diagonal CEE cut through the maximum of the RIXS pre-edge (7111.1 eV incident energy: 706.8 eV energy transfer) gives the high-resolution XANES spectrum. In addition to the main pre-edge peak at 7111.1 eV, also present in the K-edge XAS spectrum, there is a shoulder on the high-energy side of the CEE resonance at 7112.0 eV, which is not resolved in the K-edge XAS spectrum, see Figure 3a and Figure S4 in SI. The CEE cut also shows structure on the rising edge, with shoulders at 7114.2 and 7115.7 eV. The position and relative intensity of the spectral features depend on the emission energy for the CEE cut, see Figure S5 in SI, which highlights the complexity of the RIXS spectral information compared to that of the K-edge XAS.

To analyze the structure of the RIXS pre-edge and the CEE cut, the RIXS spectrum was modeled using the VBCI multiplet model with parameters originally fit to the L-edge XAS spectrum.³¹ The ground state is fully symmetric $^1A_{1g}$ (Γ_1^+ in Bethe notation), well below the first excited state (by 0.86 eV). This means that only the lowest state needs to be considered in the calculations. From the ground state there is a dominant $1s \rightarrow 3d(e_g)$ transition, leading to an E_g (Γ_3^+) state, with other quadrupole transitions having less than 3% of the intensity of the major transition, see Figure 3a. In the modeled RIXS plane, Figure 2a (bottom), this absorption resonance has two closely-lying maxima in the energy transfer direction, followed by a minor resonance at 709.7 eV, which closely reproduces the experimental data. The model CEE cut is therefore in good

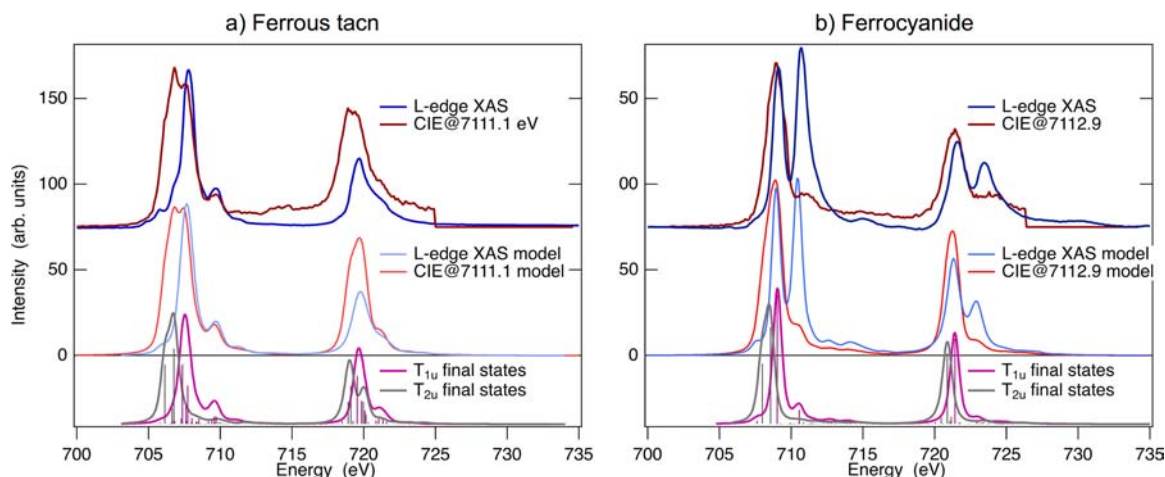


Figure 4. Comparison of the RIXS CIE cut from the maximum of the pre-edge resonance (dark red) to the L-edge XAS spectrum (dark blue) of ferrous tacn (left) and ferrocyanide (right). The results from the VBCI multiplet model are shown below the experimental results for both CIE cut (light red) and L-edge XAS (light blue). Separate contributions to the RIXS CIE spectra from final states of T_{1u} (Γ_4^-) and T_{2u} (Γ_5^-) symmetry are shown in purple and gray, respectively.

agreement with the experimental one, including the presence of a shoulder at 7112 eV. This shoulder does not correspond to any absorption resonance, and its origin can be understood by consideration of the full RIXS plane in Figure 2a (top). The CEE cut gets its major peak at 7111.1 eV from the maximum at low energy transfer (706.8 eV), but due to the large lifetime broadening in the incident energy direction, the diagonal CEE cut also has a contribution from the second emission maximum (707.6 eV), giving the shoulder at 7112 eV. The different contributions to the CEE spectrum from absorption and final-state effects illustrates the benefits of measuring the full RIXS plane^{15,76} and highlights the differences between the standard and the high-resolution XANES.^{1,15,52,68,77} To better understand the final-state effects requires a more in-depth analysis of the energy transfer spectrum.

Energy Transfer Direction. An important part of the results are the high-resolution L-edge-like spectra that can be obtained from a CIE cut through the maximum of the e_g resonance (7111.1 eV). The $2p \rightarrow 1s$ emission from the 1E_g intermediate state leads to a large number of different $2p^53d^7$ final states, and the energy difference between these states leads to a complicated emission profile with two separate maxima in the energy transfer direction, see Figure 2a. One could anticipate that, with a single dominant K pre-edge transition, the CIE cut should access almost all $2p^53d^7$ states and therefore directly correspond to the L-edge XAS spectrum. However, the direct comparison shows significant differences between the two spectra, see Figure 4a. The new features in the CIE cut are (a) larger width of both L_3 and L_2 edges with a double-peak structure in the main feature of the L_3 edge, (b) significant intensity between the edges, and (c) the appearance of broad resonance around 714 eV. From the full RIXS spectrum in Figure 2a it can be seen that both (b) and (c) originate from resonances in the rising edge, which appear in the CIE cut due to the significant lifetime broadening in the incident energy direction.

However, the increase in width of the two L-edges in the CIE cut is significant, with a fwhm of the L_3 edge of 2.4 eV in the RIXS experiment, compared to only 0.9 eV for L-edge XAS data. A separate analysis of the first resonance in ferricyanide (see the Materials and Methods section) shows that with the

present setup, hard X-ray RIXS leads to an increase in the line width of only 0.2 eV compared to that in the soft X-ray L-edge experiment. In addition, the increased line width is asymmetric to the low-energy side, which is not expected if there was a general broadening around the center of the L-edge XAS resonance. The extra width in the CIE cut must therefore originate from a fundamental difference between the two-photon RIXS process and the single-photon L-edge absorption process and not simply from a change in the experimental resolution.

To explain the difference between the two experiments, a corresponding CIE cut through the e_g resonance was made in the modeled RIXS plane, included in Figure 4a. The model reproduces the experimental findings very well, with a significantly broader L_3 edge for the RIXS CIE cut (2.2 eV fwhm) compared to the L-edge XAS (1.0 eV fwhm). The main resonance in the theoretical CIE spectrum also has a double-peak structure, a small shoulder at 706 eV and a minor peak at 709.5 eV. Note that the excellent agreement between the model and the experimental RIXS is obtained with parameters that have been fitted to the L-edge XAS spectrum only, without any further adjustments.

In the following, we show that the increased width in the CIE cut can be explained by the difference in selection rules between the single-photon L-edge XAS and the two-photon RIXS process. The latter is able to reach additional final states and the energy difference between these states leads to a broadening of the spectrum in the energy transfer direction. In both experiments the final states have a hole in a 2p orbital, and one electron in a $3d(e_g)$ orbital, see Figure S3 in SI. The 2p hole has t_{1u} symmetry, which when coupled to an e_g electron gives final states of both T_{1u} and T_{2u} symmetry, see Figure 5. However, due to the electric dipole selection rules of single-photon absorption in L-edge XAS, only final states of T_{1u} symmetry can be reached from the A_{1g} ground state in O_h symmetry, as the electric dipole operator transforms as T_{1u} . In the two-photon $K\alpha$ RIXS process, the first excitation is the electric quadrupole $1s \rightarrow 3d(e_g)$ transition, giving a doubly degenerate E_g intermediate state, from which the subsequent $K\alpha$ emission (T_{1u}) can reach final states of both T_{1u} and T_{2u} symmetry, see Figure 5.

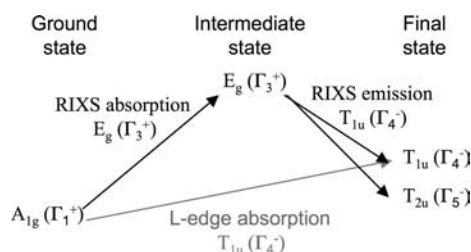


Figure 5. Relevant symmetry selection rules in O_h symmetry for $K\alpha$ RIXS and L-edge XAS from the $A_{1g}(\Gamma_1^+)$ ground state in low-spin ferrous complexes.

Separating the contributions to the modeled CIE cut by final state symmetry, which can be done directly from the original multiplet simulation without modifying any parameters, shows that the additional intensity at lower energy transfer is due to final states of T_{2u} symmetry, see Figure 4a. The energy difference between the T_{1u} and T_{2u} states can be understood in terms of electron–electron repulsion. Ignoring spin–orbit coupling, the wave function of one of T_{1u} states can be written as a product of a $2p_z$ hole and a d_z^2 electron, while the corresponding T_{2u} state is a product of a $2p_z$ hole and an electron in the $d_{x^2-y^2}$ orbital, see Figure S6 in SI. The difference in spatial overlap between the $2p$ hole and the two different e_g orbitals leads to different e^-e^- repulsion (higher for $2p_z/d_z^2$ (T_{1u})), and results in an energy splitting between final states of different symmetry and a broadening of the emission resonance. In L-edge XAS the T_{2u} state cannot be reached because the dipole transition matrix between $2p_z$ and $d_{x^2-y^2}$ orbitals is zero.⁷⁸ Other components of the T_{1u} and T_{2u} states are more complicated linear combinations of electron configurations, see Figure S6 in SI, but have the same energy and transition intensities by group theory considerations. The large number of final states instead results from the inclusion of spin–orbit coupling and additional configurations in the VBCI model.

In summary, the results for ferrous tacn show both the similarities and the differences between $K\alpha$ RIXS and L-edge XAS. An important observation is that the RIXS experiment access final states that are forbidden in the L-edge XAS experiment. The presence of these new final states introduces additional electronic structure information compared to the L-edge XAS spectrum, which shows that $K\alpha$ RIXS can be equally useful or even better than L-edge XAS for the calculation of metal–ligand covalency.

3.2. RIXS Spectrum of Ferrocyanide. Ferrocyanide is a low-spin ferrous complex (d^6), with six ligands in O_h symmetry, see Figure S1 in SI. An important difference compared to ferrous tacn is that the three occupied metal orbitals of t_{2g} symmetry interact with unoccupied π^* orbitals of the CN^- ligands, which gives rise to π -back-bonding, see Figure S7 in SI.

The $K\alpha$ RIXS spectrum of ferrocyanide is shown in Figure 2b (top). It exhibits one dominant pre-edge resonance that can be assigned to a $1s \rightarrow 3d(e_g)$ quadrupole transition. Compared to ferrous tacn, the pre-edge resonance is more compact in the energy transfer direction and has a single maximum (at 708.9 eV) instead of two separate maxima. Due to the stronger ligand field of CN^- the pre-edge resonance also appears at higher energy (7112.9 eV), placing it closer to the rising edge.

Incident Energy Direction. The K-edge XAS spectrum of ferrocyanide has significant structure along the rising edge. A fit to the to the K-edge spectrum gives, in addition to the pre-edge

resonance at 7112.9 eV, a peak at 7115.5 eV, and other more intense peaks at higher energies, see Figure S4 in SI. A CEE cut through the maximum of the pre-edge resonance (7112.9; 708.9 eV), see Figure 3, shows increased resolution compared to the K-edge XAS spectrum with a shoulder on the high-energy side of the pre-edge resonance at 7113.5 eV, although not as pronounced as in ferrous tacn. CEE cuts at other emission energies are shown in Figure S5 in SI.

A simulation of the ferrocyanide $K\alpha$ RIXS spectrum was made using the VBCI multiplet model with parameters from the previous simulation of the L-edge XAS spectrum.³² Starting from the fully symmetric $^1A_{1g}(\Gamma_1^+)$ ground state, there is a major absorption resonance at 7112.9 eV, associated with the $1s \rightarrow 3d(e_g)$ transition to an E_g intermediate state, see Figure 2b. The modeled RIXS spectrum also has a minor peak around 7114.7 eV that is not present in the ferrous tacn spectrum. A more detailed analysis shows that this resonance has two contributions, at 7114.7 and 7114.9 eV, each with different intermediate state symmetry, see Figure 3b. The intensity of both contributions increase with increasing weight of the metal-to-ligand charge transfer (MLCT) configuration in the model, see Figure S8 in SI, which shows that they stem from back-bonding. The first transition has π (T_{2g}) symmetry, see Figure 3, and corresponds to excitations into π^* metal–ligand orbitals that are consequences of π -back-bonding. The second resonance has σ (E_g) symmetry and comes from excitations into orbitals that mix the Fe d orbitals with empty ligand σ^* orbitals, i.e., σ -back-bonding, but as the d σ orbitals are unoccupied, this does not contribute to any net bonding.

Note that, although the VBCI multiplet model predicts a weak back-bonding feature, a fit to the experimental K-edge XAS spectrum gives a peak in this region with intensity similar to that of the main pre-edge peak, see Figure S4 in the SI. According to the model, a large part of the intensity must then come from transitions that do not include metal 3d orbitals. Several phenomena have been invoked to explain structure in the rising edge, e.g., transitions to empty valence states, continuum resonances with multiple back-scattering of the photoelectron,^{79,80} and multielectron excitations. As ferrocyanide is a centrosymmetric complex, metal 3d and 4p orbitals cannot mix unless vibrational coupling is considered. A likely explanation for the intense transition, based on orbital symmetry, is a transition into a predominantly $CN^- \pi^*$ orbital that has t_{1u} symmetry and mixes with the metal 4p (t_{1u}) orbitals, see Figure S7 in SI. This transition can get intensity through the electric dipole contribution and thus dominate over quadrupole transitions to metal 3d orbitals.

Energy Transfer Direction. The L_3 edge of the ferrocyanide L-edge XAS spectrum has two intense features at 709.1 and 710.7 eV with approximately equal height, see Figure 4. The second of these peaks comes from excitations into empty $CN^- \pi^*$ orbitals, and the intensity of this feature can be used to calculate the amount of π -back-bonding.³² To generate an L-edge-like spectrum, a CIE cut was made through the maximum of the main pre-edge resonance at 7112.9 eV, see Figure 4b. However, the prominent π^* peak in the L-edge XAS spectrum is very weak in the CIE cut. The other major difference is that the width of the e_g resonance increases from the 0.8 eV in the L-edge spectrum to 1.5 eV in the CIE spectrum, qualitatively similar to ferrous tacn although the change is smaller.

To analyze the differences between the two experiments, a CIE cut was made through the maximum of the modeled ferrocyanide RIXS spectrum, see Figure 4b. The model fully

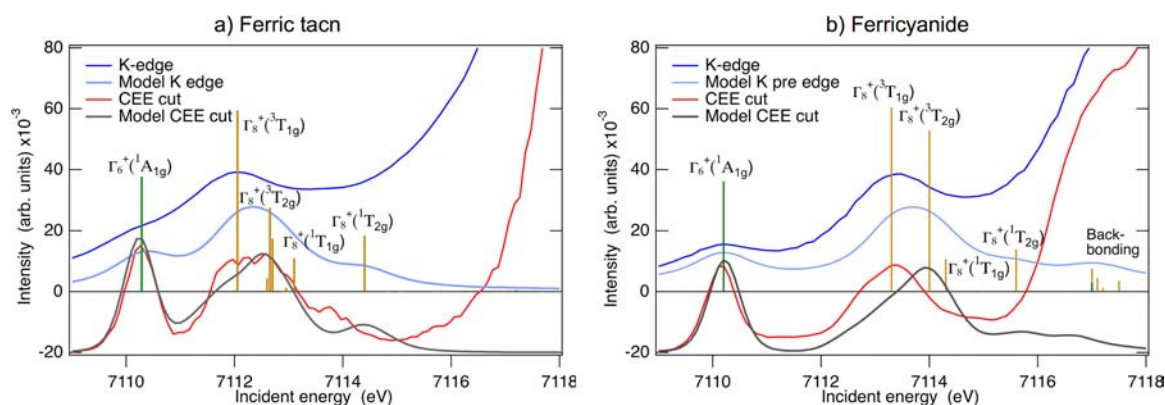


Figure 6. Spectra in the K pre-edge XAS region for ferric tacn (left) and ferrocyanide (right). Experimental K pre-edge spectra (blue) are compared to spectra from the VBCI multiplet model (light blue). Modeled absorption resonances are shown as sticks. Experimental CEE cuts through the maximum of the pre-edge resonance (red) are compared to the corresponding cuts through the modeled RIXS plane (gray). The CEE cuts are arbitrarily scaled to facilitate comparison with the K pre-edge.

reproduces the experimental observations, with an increase in width from 0.7 eV in the L-edge to 1.5 eV in the CIE cut, and low intensity at 710.7 eV where the L-edge XAS has an intense π^* resonance. As shown for ferrous tacn above, the additional width in the CIE cut is due to excitations into additional final states of T_{2u} symmetry that are allowed in the two-photon scattering process but forbidden in the single-photon X-ray absorption process, see Figure 5. A narrower CIE cut in ferrocyanide reflects a decrease in the e^-e^- repulsion that separates different states, and indicates an increased covalency in ferrocyanide relative to ferrous tacn.

The explanation for the weak π^* intensity in the ferrocyanide 7112.9 eV CIE cut is that final states corresponding to π^* transitions are mainly reached through intermediate states at 7114.7 eV, and therefore do not show up in a CIE cut taken at 7112.9 eV. In addition, the total intensity of the π^* resonance is much weaker in RIXS as compared to that for the L-edge spectrum. To explain this difference, the strong intensity in the ferrocyanide L-edge XAS spectrum is considered first. In this experiment the π^* resonance has two intensity mechanisms, direct excitation and intensity borrowing from the main resonance.³² The valence symmetry is different for excitations to 3d (e_g) and $CN^- \pi^*$ (t_{2g}) orbitals, but including the 2p hole (t_{1u}) gives final states of T_{1u} symmetry in both cases. To get intensity transfer between the final states requires both sufficient strength of the interaction that brings the states to the same symmetry, i.e., the 2p–3d interaction, and a small energy difference between the configurations.

In the K-edge absorption, coupling to the 1s hole (a_1) gives intermediate states with the same symmetry as that of the valence electron, E_g for the main transition and T_{2g} for the π^* transition. Due to the difference in symmetry, there is no borrowing mechanism, and the π^* transition in the K-edge XAS only gets intensity from the direct excitation, i.e., proportional to the d character in the π^* orbitals. If a CIE cut is made through the experimental RIXS spectrum at the predicted energy of the back-bonding peak (7114.7 eV), see Figure S9 in SI, the intensity is higher than predicted by the model, but as presented above, the majority of this intensity results from transitions to empty valence orbitals with 4p character rather than from 3d back-bonding resonances.

In summary, the significant differences between the emission spectra of ferrous tacn and ferrocyanide show that $K\alpha$ RIXS spectra are sensitive to the electronic structure, even in these

cases where the K-edge spectrum has a single pre-edge resonance. However, the relatively low intensity of the RIXS π^* resonance, together with the problem of delineating contributions from dipole-allowed transitions in the K-edge XAS, makes it less straightforward to use $K\alpha$ RIXS relative to the L-edge XAS to quantify the amount of π back-bonding. The difference in intensity mechanisms for the π^* resonance, and the presence of T_{2u} states in RIXS but not in the L-edge XAS, makes the two experiments complementary in assigning the electronic structure of ferrocyanide.

3.3. RIXS Spectrum of Ferric tacn. Ferric tacn is a six-coordinated low-spin d^5 complex, see Figure S1 in SI. In O_h symmetry a low-spin ferric complex is subject to a weak Jahn–Teller distortion, and as the ligand environment is not fully symmetric, this results in formal C_2 symmetry, with calculated metal–ligand distances between 2.028 and 2.036 Å. However, as the distortions are small O_h symmetry has been used throughout this analysis.

The $K\alpha$ RIXS spectrum of ferric tacn is given in Figure 2c (top). It shows two distinct features in the pre-edge that are both very different in shape compared to the pre-edge resonance of ferrous tacn. The first feature, located at an incident energy of 7110.3 eV, is very sharp in the energy transfer direction, while the second one, with a maximum at 7112.4 eV, is much broader in both the incident energy and energy transfer directions. To understand the structure of the RIXS spectrum, the K-edge spectrum is considered first, followed by an analysis of the energy transfer dimension.

Incident Energy Direction. A fit to the K pre-edge of ferric tacn gives a peak at 7110.2 eV, while the broad resonance fits two peaks at 7111.5 and 7112.5 eV. In addition, there seems to be an additional peak at 7113.5 eV, see Figure S4 in SI. The CEE cut through the maximum of the first resonance is displayed in Figure 6, while CEE cuts at other energies are shown in Figure S5 in SI. The first resonance is very sharp in the CEE cut, while the second resonance shows significant structure. There is also a third weak feature at 7113.8 eV.

To understand the shape and origin of the pre-edge resonances, the $K\alpha$ RIXS spectrum of ferric tacn was simulated using the VBCI multiplet model, see Figure 2c (bottom). The electron configuration in the ground state is t_{2g}^5 and this $^2T_{2g}$ state splits into Γ_7^+ ($J' = 1/2$) and Γ_8^+ ($J' = 3/2$) spin–orbit components.³² Γ_7^+ is lower than Γ_8^+ by 0.1 eV, and this energy difference is large enough so that only the Γ_7^+ state has any

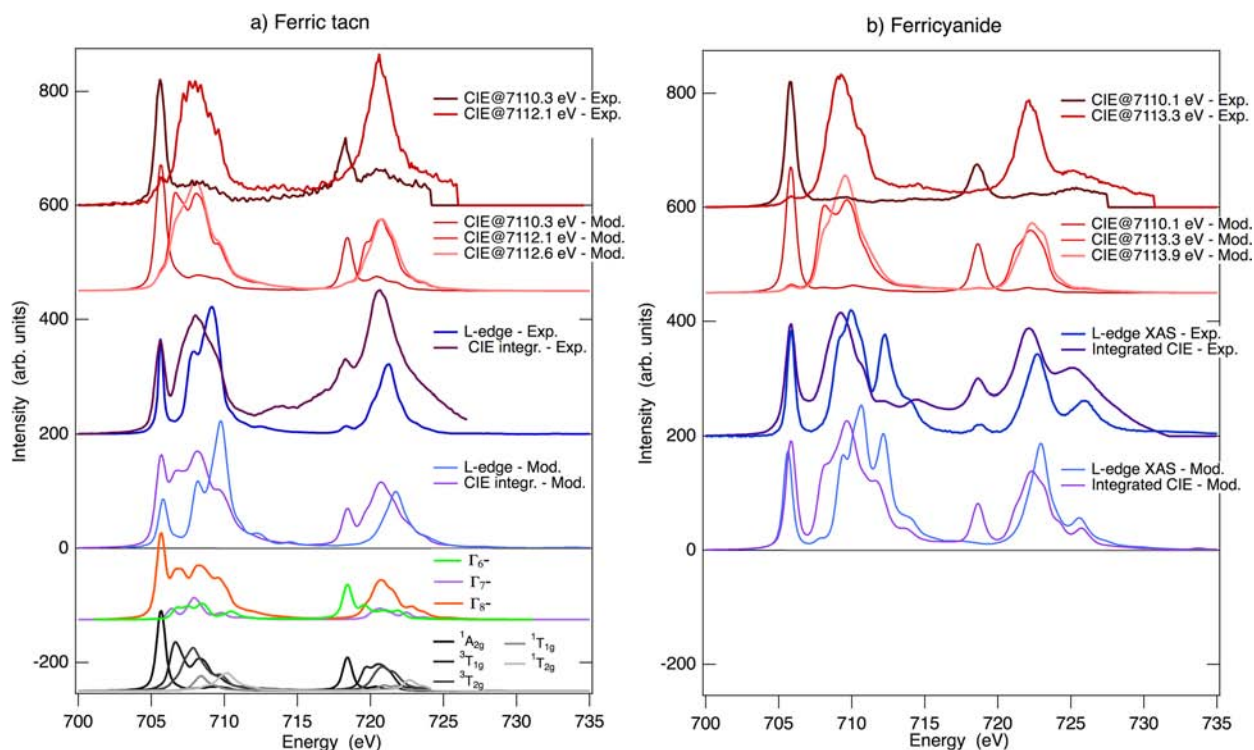


Figure 7. Experimental and modeled CIE cuts through the center of the pre-edge features, together with integrated CIE spectra (purple) and L-edge XAS (blue) for ferric tacn (left) and ferrocyanide (right). The integrations of the experimental CIE spectra are done up to an incident energy of 7115.0 eV for ferric tacn and 7114.3 eV for ferricyanide to limit the effects from the rising edge. Contributions to the integrated CIE spectrum of ferric tacn from final states of different symmetry are shown in light green (Γ_6^-), violet (Γ_7^-), and orange (Γ_8^-), and contributions from different intermediate states, labeled by the symmetry of the valence state, are shown at the bottom.

significant thermal population even if the experiments would be performed at room temperature ($kT = 25$ meV).

According to the model, the first absorption resonance at 7110.2 eV is an excitation from $1s$ to fill the hole in the t_{2g} shell, which leads to a the coupling of a $1s$ hole (${}^2A_{1g}$) to a fully symmetric ${}^1A_{1g}$ valence state that combines to a ${}^2A_{1g}$ (Γ_6^+) intermediate state, see Figure 6. Next comes contributions from $1s \rightarrow 3d(e_g)$ excitations, whose orbital occupancy of $1s^1 t_{2g}^5 e_g^1$, see Figure S10 in SI, gives states corresponding to the coupling of the $1s$ hole to ${}^3T_{1g}$, ${}^3T_{2g}$, ${}^1T_{1g}$, ${}^1T_{2g}$ valence states of the $t_{2g}^5 e_g^1$ configuration, see Figure S11 in SI, giving intermediate states of Γ_8^+ symmetry.⁴ The broad pre-edge feature includes the ${}^3T_{1g}$, ${}^3T_{2g}$, and ${}^1T_{1g}$ valence states, while the minor absorption resonance at 7113.5 eV is matched to the ${}^1T_{2g}$ state, see Figure 6. The modeled CEE spectrum gives a reasonable match to the experimental spectrum, with a correct shape of the first pre-edge resonance but the intensity of the transitions to the e_g orbitals are underestimated at lower incident energies and the ${}^1T_{2g}$ valence state appears at too high an energy.

Energy Transfer Direction. The difference in shape between the different ferric tacn RIXS resonances in Figure 2c (middle) suggests that significant information can be extracted from the high-resolution L-edge-like spectra. For this purpose, CIE cuts were taken through the center of the different pre-edge resonances at 7110.3 and 7112.1 eV respectively, see Figure 7a.

The CIE cut through the first resonance probes the emission from the t_{2g} resonance that corresponds to the $1s^1 t_{2g}^6$ intermediate state. This leads to the $2p^5 t_{2g}^6$ final state, and gives a sharp peak at 705.6 eV with a fwhm of 0.8 eV, and a broad, less intense feature, around 708 eV (dark-red line in Figure 7a). Compared to the experimental L-edge XAS

spectrum (dark-blue line), the L_3 resonance appears very similar, but the L_2 resonance is more intense in the RIXS data.

The multiplet model reproduces the experimental t_{2g} CIE cut, including the higher intensity of the t_{2g} L_2 peak as compared to L-edge XAS. The emission spectra are sharp because in the $2p^5 t_{2g}^6$ final state, the $2p$ hole interacts with subshells that are either completely filled or empty, and there is no multiplet splitting. The difference between RIXS CIE and L-edge XAS can again be explained by a difference in selection rules. As explained in reference,³² the t_{2g} L_2 final state has Γ_6^- symmetry (green line in Figure 7a), and cannot be reached by electric dipole transitions (Γ_4^-) from the Γ_7^+ ground state, see Figure 8. The minor intensity that appears in the L-edge XAS spectrum comes from distortions to lower symmetry. However, the two-photon RIXS experiment does reach Γ_6^- final states through $1s \rightarrow 3d(t_{2g})$ quadrupole absorption (Γ_5^+) followed by electric dipole $K\alpha$ emission, see Figure 8

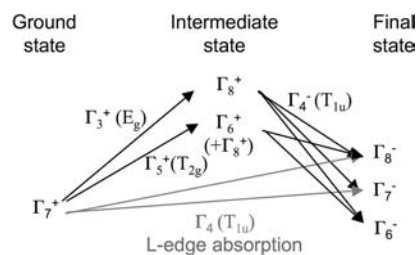


Figure 8. Relevant symmetry selection rules in O_h symmetry for $K\alpha$ RIXS and L-edge XAS from the Γ_7^+ ground state of low-spin ferric complexes.

A cut through the maximum of the experimental e_g resonance at 7112.1 eV (red line in Figure 7a) shows a broad structure in the energy transfer direction. For this value of the incident energy the L_2 edge has higher intensity than the L_3 edge, but the shape of the resonances and the L_3/L_2 ratio varies with energy, see Figure S12 in SI. For systems with multiple pre-edge resonances, the sensitivity to both incident and emission energy makes it difficult to analyze individual CIE cuts.

An alternative is to sum the CIE cuts over all incident energies, giving an integrated CIE spectrum (purple line in Figure 7a). Unlike the individual CIE cuts, this representation contains all $2p^53d^6$ final states and shows how the total intensity is distributed over the energy transfer axis, which is required for a direct comparison with the L-edge XAS spectrum. The integrated CIE spectra also preserve the high resolution in the energy transfer direction for isolated resonances, as can be seen by the sharp t_{2g} resonance. However, at higher energy transfer values there are significant contributions from the rising edge, which distorts the shape of the L_2 edge.

For ferric tacn the overall shape of the e_g resonance in the integrated CIE spectrum changes significantly compared to the L-edge XAS spectrum (dark blue line in Figure 7a). The RIXS-derived spectrum has maximum intensity at 708 eV, with a shoulder at 709 eV, while in the L-edge XAS there is a minor peak at 708 eV and a maximum at 709 eV. Furthermore, the gap between the t_{2g} and e_g resonances is smaller in the integrated CIE spectrum due to significant intensity between 706 and 707 eV energy transfer.

The widening of the e_g resonance toward lower energy transfer values resembles the situation for the low-spin ferrous complexes. For these complexes, the broadening was a consequence of additional final states in the two-photon RIXS process that could not be reached in the single-photon L-edge XAS experiment. For low-spin ferric complexes, RIXS gives access to Γ_6^- states that are not allowed in L-edge XAS, see Figure 8. However, an analysis of the symmetry contributions to the integrated CIE spectra shows that final states of Γ_8^- symmetry, formally allowed also in the L-edge XAS process, dominate the new contributions in the 706–707 eV region, see Figure 7a.

Instead plotting the contributions by their intermediate state shows that the 706–707 eV energy transfer region is mainly reached from the $^3T_{1g}$ intermediate state, see Figure 7a. As the intensities of the “triplet” intermediates are much higher than the “singlet” intermediates in the K-edge absorption process, see Figure 6, the energy region in RIXS associated with these transitions gets relatively high intensity. This is another example of how strongly the RIXS spectrum is affected by the interactions in the intermediate state.

These results for ferric tacn further illustrate the similarities and differences between $K\alpha$ RIXS and L-edge spectra. The similarity in shape and line width of the t_{2g} peak in the L_3 edge shows that high-resolution L-edge-like spectra can be obtained using hard X-rays, and the high resolution is preserved for well-isolated resonances when integrating the CIE spectra to include all $2p^53d^6$ final states. The change in shape and width of the e_g resonance again reflects the difference in selection rules between the two methods. As was the case for the low-spin ferrous complexes, the RIXS experiment accesses final states that are forbidden in the L-edge XAS experiment, and these states provide additional information about the electronic structure.

3.4. RIXS Spectrum of Ferricyanide. Ferricyanide combines features from the previously analyzed complexes, i.e., the effects of back-bonding associated with the cyanide ligands, as well as the t_{2g} hole and the multiple pre-edge resonances of low-spin ferric complexes. The system has D_{4h} symmetry due to a weak Jahn–Teller distortion and according to DFT calculations two Fe–ligand distances are 1.958 Å (in trans positions) while the other four are 1.963 Å. This distortion only leads to a small splitting of the t_{2g} level (≤ 2.4 meV) and ferricyanide has been modeled using O_h symmetry.

The RIXS spectrum of ferricyanide is shown in Figure 2d. It exhibits similar t_{2g} and e_g resonances as ferric tacn, with a sharp t_{2g} resonance in the energy transfer direction while the e_g resonance is broad in both incident and energy transfer directions. The clearest difference between the two low-spin ferric complexes is that the separation between the t_{2g} and e_g pre-edge resonances are larger in ferricyanide, which results from a larger ligand field splitting.

Incident Energy Direction. The K pre-edge spectrum of ferricyanide shows two peaks, corresponding to the t_{2g} and main e_g resonances, and significant structure along the rising edge with intense resonances at 7117 eV and above, see Figure 6. A CEE cut through the maximum of the t_{2g} resonance (7110.1; 705.8 eV) gives a well-resolved picture of the rising edge, and clearly shows the difference in structure between the t_{2g} and e_g , see Figure 6. CEE cuts at other emission energies are shown in Figure S5 in SI.

As for the other complexes, the RIXS process was modeled with the multiplet model using parameters from a previous L-edge XAS simulation.³² The ground state is Γ_7^+ ($J' = 1/2$) with a Γ_8^+ ($J' = 3/2$) state 0.1 eV higher in energy. The modeled K-edge absorption spectrum has the same features as that of ferric tacn: a t_{2g} excitation, a group of resonances from the e_g excitation that corresponds to the $^3T_{1g}$, $^3T_{2g}$ and $^1T_{1g}$ valence states, and a $^1T_{2g}$ valence state at higher energy, see Figure 6. In addition, there are transitions at 7117.4 eV that are not present in ferric tacn. An analysis of the K pre-edge absorption spectrum shows that the intensity of this high-energy feature increases with increasing weight of the MLCT configuration, see Figure S8 in SI, which indicates that it arises from back-bonding. Note that intensity borrowing between e_g and π^* resonances in the intermediate state are not strictly forbidden because they both have Γ_8^+ symmetry, see Figure 6. However, the 3d spin–orbit coupling that connect these states is small compared to the energy difference and the π^* feature remains weak.

A CEE cut through the modeled t_{2g} resonance reproduces the main features of the experimental spectrum, e.g., the difference in shape of the main pre-edge resonances and the large splitting between the t_{2g} and e_g resonances. However, the model spectrum overestimates the intensity at higher incident energies, with a maximum at 7113.9 eV compared to 7113.3 eV in the experimental spectrum, see Figure 6. The calculated energy of the back-bonding peak coincides with an intense feature in the K-edge XAS spectrum at 7117 eV, see Figure 6, but as the modeled intensities of the back-bonding transitions are small, only 8% of the total quadrupole intensity, a majority of this intensity in the K-edge XAS must originate from other sources than quadrupole transitions. As for ferrocyanide, a reasonable explanation for this intensity would be excitations into a predominantly ligand orbital of t_{1u} symmetry, which get intensity by mixing with the metal 4p orbitals.

Energy Transfer Direction. CIE cuts taken through the center of the different pre-edge resonances are shown in Figure 7b. The CIE cut through the RIXS t_{2g} resonance at 7110.1 eV gives two sharp edges, while the CIE cut through the e_g resonance at 7113.3 eV shows a broad features with a width of 2.7 eV in the L_3 edge, slightly smaller than the corresponding value for ferric tacn (3.1 eV). CIE cuts at other incident energies are shown in Figure S12 in SI.

A comparison of the integrated CIE and the L-edge XAS shows similar differences as in ferric tacn, i.e., a change in shape of the e_g resonance with significant additional intensity at lower final state energies and a more intense t_{2g} L_2 edge. As for the complexes studied above, the additional intensity is due to excitations into final states that are either forbidden or have very low intensity in the direct L-edge excitation. The π -back-bonding feature in the L-edge XAS spectrum is not seen in the integrated CIE spectrum because the back-bonding peak in the K-edge appears at 7117 eV according to the model, and this energy is not included in the integration due to the large contribution from the rising edge. The total intensity of the back-bonding feature is also predicted to be much lower in RIXS than in L-edge XAS.

Ferricyanide thus confirms the more detailed analysis of the other complexes, i.e., the more complicated pre-edge structure of a low-spin ferric system, the presence of additional final states in RIXS and a weak π -back-bonding feature overlapped by other more intense transitions in the rising edge. Despite a general agreement between the model and the experimental results, there are some quantitative differences. This suggests that a better fit of the VBCI model could possibly be obtained by using the RIXS data in the fitting procedure.

3.5. VBCI Parameters from Spectral Fits. One goal of the present combination of $K\alpha$ RIXS experiments and VBCI multiplet modeling is to extract metal–ligand covalencies for systems where only RIXS data are available. This requires that the modeled spectrum is accurate, sensitive to the parameters that determine covalency, and that there is a unique solution to the fitting procedure. To evaluate how well these criteria are fulfilled, the RIXS spectra of all four complexes have been simulated by varying the model parameters.

Ferrous Complexes. The presence of a single dominant pre-edge resonance in the low-spin ferrous complexes means a single CIE cut can be used to represent the full RIXS spectrum. The ferrous tacn CIE cut has a double-peak structure in the L_3 -edge, with the low-energy peak slightly higher in intensity than the high-energy peak, see Figure 4a. The VBCI simulation of ferrous tacn with the original L-edge XAS parameters³¹ reproduces the width and double-peak structure of the peak, but with an almost equal intensity of the two peaks, see Figure 4. If the parameters are fit directly to the CIE cut, a better match is achieved by decreasing the e_g covalency by 2–4%, e.g., by lowering the mixing parameter $T(e_g)$ from 1.8 to 1.6 eV, see Figure S13 in SI. Metal–ligand covalencies calculated from the VBCI model fit to RIXS data are given in Table S3 in the SI. The sensitivity of the CIE spectrum to the model parameters suggests that it is a good probe of electronic structure. A comparison of simultaneous RIXS and L-edge XAS simulations, see Figure S13 in SI, shows that the RIXS CIE cut is actually more sensitive to the electronic structure because the final states of T_{2u} symmetry add an additional dimension that can be used in the analysis.

However, both the modeled L-edge spectrum and the CIE cut are also affected by the t_{2g} covalency and the strength of the

ligand field, see Figure S13 in SI. As an example, simultaneously increasing the ligand field strength by 0.3 eV and decreasing the e_g covalency by 5% also gives a good fit to the experimental CIE spectrum. For systems like ferrous tacn, where there are multiple solutions to the fitting procedure, a more reliable fit can be obtained by using a reasonable starting value for the ligand field strength from other spectroscopic data.³² For complexes where both RIXS and L-edge XAS data are available, the use of two different data sets should in general improve the fitting procedure compared to the situation with only L-edge XAS data.

The ferrocyanide CIE cut was almost 1.0 eV narrower than the corresponding resonance for ferrous tacn. The multiplet model reproduces this difference, but changing the amount of σ and π -bonding in the ferrous tacn model mainly affects the shape, not the width of the spectrum, see Figure S13 in SI. To match the relatively narrow peak width of ferrocyanide requires the introduction of a significant amount of back-bonding, i.e., increasing the weight of the MLCT configuration in the three-configuration model, see Figure S14 in SI. This means that although the e_g CIE cut does not probe the π^* orbitals directly, the indirect effects of π -back-bonding are large enough to be detected in the e_g CIE cut. However, the L-edge is still a more sensitive probe of π -back-bonding because a small increase in the weight of the MLCT configuration has a large effect on the intensity of the π^* resonance, see Figure S14 in SI.

Ferric Complexes. For systems with multiple pre-edge resonances that can only be investigated using hard X-rays, an attractive alternative would be to fit the VBCI model directly to the K-edge XAS spectrum instead of performing the more complicated $K\alpha$ RIXS experiment. However, as shown in Figure S15 in SI, the energies and intensities of the K pre-edge transitions are not very sensitive to the metal–ligand covalency, making it difficult to extract the 3d covalency from the X-ray absorption spectrum only.

Fits to the integrated CIE spectrum reveal that the results are sensitive to small changes in the VBCI model parameters, see Figure S16 in SI. As an example, an increase in the e_g covalency decreases the e^-e^- repulsion, the energy difference between different e_g final states, and thus the intensity between the t_{2g} and e_g resonances. In general, the match between experimental and modeled spectra is not as good as for the ferrous complexes, possibly due to the added complexity of a large number of intermediate states, each with very different emission spectra. No improvement in the fit can be achieved by changing the t_{2g} and e_g mixing parameters relative to their original values from the L-edge XAS. However, the sensitivity of the spectra to model parameters indicates that the spectral data can be used to probe electronic structure, and this is important regardless of the quality of the final fit.

Comparing the integrated CIE spectra of ferric tacn and ferrocyanide, shows that although there are some differences in the shape of the e_g resonance, see Figure S17 in SI, there is no clear difference in the width of the e_g resonance. Multiplet modeling of ferrocyanide with different weight of the MLCT configuration confirms that the width of the e_g resonance is not very sensitive to the amount of back-bonding, see Figure S18 in SI. This makes it difficult to fit the back-bonding parameters of ferrocyanide to only the integrated CIE spectrum. The different behavior compared to ferrocyanide is likely due to the fact that the width of the e_g resonance in the integrated CIE spectrum ferrocyanide is affected by the presence of multiple e_g transitions with different energy.

4. DISCUSSION

Development of better catalysts, whether inspired from biological systems or through inorganic syntheses, requires knowledge about the electronic structure of the metal 3d orbitals involved in metal–ligand bonding and catalysis. In the present study the electronic structures, in particular the metal–ligand covalencies, of four iron complexes have been obtained by a combination of $K\alpha$ RIXS to get high energy-resolution X-ray spectra, and VBCI modeling to extract the covalency information from these feature-rich spectra.

As the electron configuration in the final state is the same in $K\alpha$ RIXS and in L-edge XAS spectra, which has previously been used to quantify metal–ligand bonding,^{31,32} the two approaches have been thoroughly compared to one another. An important observation is that for all complexes, there are additional final states that are allowed in two-photon RIXS but symmetry-forbidden in the single-photon L-edge XAS process, see Figure 5 and Figure 8. The energy differences between these final states determines the shape and the width of the energy transfer spectrum, which in turn can be used to fit the metal–ligand covalency using the multiplet model without information from any previous L-edge XAS experiment.

For systems with π -back-bonding, the relatively low intensities for direct excitations into the π^* orbitals, together with the problem of separating the 3d– π^* contributions from other contributions to the rising K edge, i.e., metal 4p mixing, complicates the assignment. However, for ferrocyanide the energy transfer spectrum from the main e_g resonance is still sensitive to the amount of back-bonding, and can be used to quantify this through VBCI modeling.

An important consideration is that a successful fitting procedure requires a high-resolution experimental setup that preserves the detailed spectral information, i.e., with an experimental resolution close to the lifetime broadening of the iron L_3 edge (0.4 eV). Another important point is that an unrestricted multiparameter fit to a single spectrum is not necessarily unique. As an example, for a calculation of the metal–ligand covalency of ferrous tacn to be stable within $\pm 5\%$ requires the ligand field splitting to be estimated within 0.3 eV. Reasonable starting parameters must therefore be obtained from electronic structure calculations, previous VBCI modeling of a related model complex, or in particular, absorption spectroscopic data.

The $K\alpha$ RIXS approach can be applied to any biological or inorganic catalytic system but is most useful for systems that cannot be probed by UV/vis or soft X-ray spectroscopy. One potentially important area is heme enzymes, e.g., cytochrome P450 and cytochrome c. These have been studied using the intense $\pi \rightarrow \pi^*$ transitions in the porphyrin to detect intermediates, but much of the insight into their electronic structure and its contribution to reactivity has had to come from calculations, as the intense ligand features obscure the Fe center. Another possible application can be in the analysis of the electronic structure of transition-metal catalysts in solar energy systems, where the chromophores designed to absorb visible light obscure many spectral probes of the catalyst itself.

For systems that are preferably probed by hard X-rays, a number of experimental alternatives to $K\alpha$ RIXS can also be considered. The K pre-edge XAS spectrum can in principle be used to assign metal–ligand covalency for systems with multiple pre-edge peaks, but the low sensitivity of energies and intensities to the metal–ligand covalency, see Figure S15,

makes it difficult to fit the electronic structure parameters only to the K pre-edge data. Nonresonant X-ray Raman spectroscopy directly gives high-resolution L-edge like spectra using hard X-rays, but due to the lack of resonance enhancement the iron signal could be difficult to distinguish from the background, and the required radiation dose is expected to be high compared to $K\alpha$ RIXS. An experimental approach that has already been successfully applied to enzyme systems is $K\beta$ valence X-ray emission.^{81,82} This method gives sensitive information about the nature of the ligands, primarily through mixing with the metal p orbitals. The information is complementary to that from $K\alpha$ RIXS, which primarily probes the interactions between the ligand valence orbitals and the metal 3d orbitals that determine the bonding. Among hard X-ray methods, $K\alpha$ RIXS can thus give unique insight into the connection between reactivity and metal–ligand bonding.

For transition-metal systems where soft X-ray L-edge XAS data can be measured, a number that will increase with the development of solution cells for vacuum setups, the $K\alpha$ RIXS spectrum still provides valuable information. The difference in selection rules and intensity mechanisms between the two experiments can be used to assign unknown spectral features, even without the use of a parametrized model. Simultaneous fitting of data from two experimental techniques also limits the parameter space for systems where different sets of parameters give equally good fits to one type of spectrum. For the present study of high-symmetry complexes, the addition of RIXS data did not significantly improve the parameters from the L-edge XAS fitting, but the situation could be different for systems of lower symmetry because the number of model parameters increases with decreasing symmetry.

This extensive investigation of ferrous and ferric tacn and the hexacyanides has primarily been motivated by their use as well-known benchmarks, but despite the wealth of previous information from other spectroscopies, e.g., vibration and UV/vis spectroscopy, L-edge XAS and RIXS are uniquely able to separate and quantify the effects of σ -donation, π -donation and the π -back-donation. This demonstrates their value as direct probes of 3d metal–ligand bonding, also for systems that can be probed using more conventional UV/vis absorption spectroscopy. With a growing number of experimental stations capable of high-resolution X-ray spectroscopy, the combination of $K\alpha$ RIXS with a theoretical model to extract electronic structure should therefore be of great use for a wide range of transition metal complexes.

5. CONCLUSIONS

$K\alpha$ RIXS involves $1s \rightarrow 3d$ excitation and detection of the $2p \rightarrow 1s$ ($K\alpha$) emission. This two-photon process reaches similar final states as in single-photon L-edge ($2p \rightarrow 3d$) X-ray absorption spectroscopy (XAS), but involves only hard X-rays. Therefore, $K\alpha$ RIXS can be used to get L-edge-like spectra for metalloproteins and solution catalysts using a high energy-resolution setup. The RIXS data can then be used to obtain metal–ligand covalencies without previous information from an L-edge XAS experiment. To obtain an accurate determination of covalency using the VBCI multiplet model, a good estimate of the ligand field strength is required, information that can be obtained either from optical spectroscopy or theoretical calculations.

For systems where L-edge data are available, the differences in selection rules between $K\alpha$ RIXS and L-edge XAS make them complementary in assigning electronic structure. Good

examples are the π -back-bonding features in ferro- and ferricyanide that are significantly more intense in the L-edge XAS as compared to $K\alpha$ RIXS, and the presence of final states reached in the two-photon RIXS process but forbidden in single-photon L-edge XAS. The simultaneous fitting of the model parameters to two different types of X-ray spectra also increases the reliability of the spectral fit, which can be important in quantifying the covalencies in systems of lower symmetry.

The present $K\alpha$ RIXS approach should thus be of great utility for many catalytic systems, either as a stand-alone method, in tandem with L-edge XAS for strongly covalent systems that are difficult to probe by UV/vis spectroscopy, or as an extension to conventional absorption spectroscopy for a wide range of transition metal enzymes and catalysts.

■ ASSOCIATED CONTENT

■ Supporting Information

Details of RIXS photodamage studies, energy calibration and intensity normalization. Additional details of the L-edge XAS and RIXS VBCI multiplet simulations. Analysis of the effects of deviations from O_h symmetry. Covalencies from VBCI modeling and DFT calculations. Details of the VBCI parameter fit to K-edge XAS data for ferric complexes. Additional figures S1–S18. Complete reference 73. This material is available free of charge via the Internet at <http://pubs.acs.org>.

■ AUTHOR INFORMATION

Corresponding Authors

bhedman@stanford.edu
hodgsonk@stanford.edu
edward.solomon@stanford.edu

Present Addresses

^{||}Department of Chemistry - Ångström, Uppsala University, SE-751 20 Uppsala, Sweden.

[†]Max Planck Institute for Chemical Energy Conversion, D-45470 Mülheim, Germany and Cornell University, Department of Chemistry and Chemical Biology, Ithaca, NY 14853, United States.

Notes

The authors declare no competing financial interest.

■ ACKNOWLEDGMENTS

We thank Frank de Groot for assistance in RIXS modeling, Patrick Frank for helpful discussions and Matthew Latimer, Xuena Zhang, Roberto Alonso Mori, Dimosthenis Sokaras and Tsu-Chien Weng for their assistance with the RIXS experiments at SSRL BL6-2. M.L. acknowledges the Marcus and Amalia Wallenberg foundation for a postdoctoral scholarship, the “Stig Hagström Stipend” and T.K. for financial support by the German Research Foundation (DFG) Grant KR3611/2-1. The research was supported by NIH Grant GM40392 (EIS), NCR RR-01209, and GM103393. Portions of this research were carried out at BL6-2 at the Stanford Synchrotron Radiation Lightsource (SSRL), a Directorate of SLAC National Accelerator Laboratory and an Office of Science User Facility operated for the U.S. Department of Energy (DOE) Office of Science by Stanford University. The SSRL Structural Molecular Biology Program is supported by the DOE Office of Biological and Environmental Research, and by the National Institutes of Health, National Institute of General Medical Sciences (including P41GM103393). Experiments were also performed

on the ID26 beamline at the European Synchrotron Radiation Facility (ESRF), Grenoble, France.

■ REFERENCES

- (1) Glatzel, P.; Bergmann, U. *Coord. Chem. Rev.* **2005**, *249*, 65–95.
- (2) Ament, L. J. P.; van Veenendaal, M.; Devereaux, T. P.; Hill, J. P.; van den Brink, J. *Rev. Mod. Phys.* **2011**, *83*, 705–767.
- (3) Hahn, J. E.; Scott, R. A.; Hodgson, K. O.; Doniach, S.; Desjardins, S. R.; Solomon, E. I. *Chem. Phys. Lett.* **1982**, *88*, 595–598.
- (4) Westre, T. E.; Kennepohl, P.; DeWitt, J. G.; Hedman, B.; Hodgson, K. O.; Solomon, E. I. *J. Am. Chem. Soc.* **1997**, *119*, 6297–6314.
- (5) Wilke, M.; Farges, F.; Petit, P. E.; Brown, G. E.; Martin, F. *Am. Mineral.* **2001**, *86*, 714–730.
- (6) Smolentsev, G.; Soldatov, A. V.; Messinger, J.; Merz, K.; Weyhermüller, T.; Bergmann, U.; Pushkar, Y.; Yano, J.; Yachandra, V. K.; Glatzel, P. *J. Am. Chem. Soc.* **2009**, *131*, 13161–13167.
- (7) Lee, N.; Petrenko, T.; Bergmann, U.; Neese, F.; DeBeer, S. *J. Am. Chem. Soc.* **2010**, *132*, 9715–9727.
- (8) Gel'mukhanov, F.; Ågren, H. *Phys. Rep.* **1999**, *312*, 87–330.
- (9) Kotani, A.; Shin, S. *Rev. Mod. Phys.* **2001**, *73*, 203–246.
- (10) Kao, C.-C.; Caliebe, W.; Hastings, J.; Gillet, J.-M. *Phys. Rev. B* **1996**, *54*, 16361–16364.
- (11) Butorin, S. M.; Mancini, D. C.; Guo, J. H.; Wassdahl, N.; Nordgren, J.; Nakazawa, M.; Tanaka, S.; Uozumi, T.; Kotani, A.; Ma, Y.; Myano, K. E.; Karlin, B. A.; Shuh, D. K. *Phys. Rev. Lett.* **1996**, *77*, 574–577.
- (12) Butorin, S. M.; Guo, J. H.; Magnuson, M.; Kuiper, P.; Nordgren, J. *Phys. Rev. B* **1996**, *54*, 4405–4408.
- (13) Platzman, P. M.; Isaacs, E. D. *Phys. Rev. B* **1998**, *57*, 11107–11114.
- (14) Hämäläinen, K.; Siddons, D. P.; Hastings, J. B.; Berman, L. E. *Phys. Rev. Lett.* **1991**, *67*, 2850–2853.
- (15) Carra, P.; Fabrizio, M.; Thole, B. *Phys. Rev. Lett.* **1995**, *74*, 3700–3703.
- (16) De Groot, F. *Chem. Rev.* **2001**, *101*, 1779–1808.
- (17) Glatzel, P.; Sikora, M.; Smolentsev, G.; Fernandez-Garcia, M. *Catal. Today* **2009**, *145*, 294–299.
- (18) Hayashi, H.; Takeda, R.; Udagawa, Y.; Nakamura, T.; Miyagawa, H.; Shoji, H.; Nanao, S.; Kawamura, N. *Phys. Rev. B* **2003**, *68*, 045122-(1–9).
- (19) Lu, L.; Hancock, J. N.; Chabot-Couture, G.; Ishii, K.; Vajk, O. P.; Yu, G.; Mizuki, J.; Casa, D.; Gog, T.; Greven, M. *Phys. Rev. B* **2006**, *74*, 224509-(1–9).
- (20) Forte, F.; Ament, L. J.; van den Brink, J. *Phys. Rev. Lett.* **2008**, *101*, 106406-(1–4).
- (21) Glatzel, P.; Bergmann, U.; Yano, J.; Visser, H.; Robblee, J. H.; Gu, W. W.; de Groot, F. M. F.; Christou, G.; Pecoraro, V. L.; Cramer, S. P.; Yachandra, V. K. *J. Am. Chem. Soc.* **2004**, *126*, 9946–9959.
- (22) Leidel, N.; Chernev, P.; Havelius, K. G.; Schwartz, L.; Ott, S.; Haumann, M. *J. Am. Chem. Soc.* **2012**, *134*, 14142–14157.
- (23) de Groot, F. M. F.; Glatzel, P.; Bergmann, U.; van Aken, P. A.; Barrea, R. A.; Klemme, S.; Havecker, M.; Knop-Gericke, A.; Heijboer, W. M.; Weckhuysen, B. M. *J. Phys. Chem. B* **2005**, *109*, 20751–20762.
- (24) Kas, J. J.; Rehr, J. J.; Soininen, J. A.; Glatzel, P. *Phys. Rev. B* **2011**, *83*, 235114-(1–10).
- (25) Glatzel, P.; Bergmann, U.; Gu, W. W.; Wang, H. X.; Stepanov, S.; Mandimutsira, B. S.; Riordan, C. G.; Horwitz, C. P.; Collins, T.; Cramer, S. P. *J. Am. Chem. Soc.* **2002**, *124*, 9668–9669.
- (26) Kotani, A.; Okada, K.; Vanko, G.; Dhalenne, G.; Revcolevschi, A.; Giura, P.; Shukla, A. *Phys. Rev. B* **2008**, *77*, 205116-(1–11).
- (27) Yang, W. L.; Sorini, A. P.; Chen, C. C.; Moritz, B.; Lee, W. S.; Vernay, F.; Olalde-Velasco, P.; Denlinger, J. D.; Delley, B.; Chu, J. H.; Analytis, J. G.; Fisher, I. R.; Ren, Z. A.; Yang, J.; Lu, W.; Zhao, Z. X.; van den Brink, J.; Hussain, Z.; Shen, Z. X.; Devereaux, T. P. *Phys. Rev. B* **2009**, *80*, 014508-(1–10).
- (28) Krause, M. O.; Oliver, J. H. *J. Phys. Chem. Ref. Data* **1979**, *8*, 329–338.
- (29) de Groot, F. *Coord. Chem. Rev.* **2005**, *249*, 31–63.

- (30) Ikeno, H.; de Groot, F. M. F.; Stavitski, E.; Tanaka, I. *J. Phys.: Condens. Matter* **2009**, *21*, 104208–(1–17).
- (31) Wasinger, E. C.; de Groot, F. M. F.; Hedman, B.; Hodgson, K. O.; Solomon, E. I. *J. Am. Chem. Soc.* **2003**, *125*, 12894–12906.
- (32) Hocking, R. K.; Wasinger, E. C.; de Groot, F. M. F.; Hodgson, K. O.; Hedman, B.; Solomon, E. I. *J. Am. Chem. Soc.* **2006**, *128*, 10442–10451.
- (33) Hocking, R. K.; Wasinger, E. C.; Yan, Y. L.; deGroot, F. M. F.; Walker, F. A.; Hodgson, K. O.; Hedman, B.; Solomon, E. I. *J. Am. Chem. Soc.* **2007**, *129*, 113–125.
- (34) Hocking, R. K.; DeBeer George, S.; Gross, Z.; Walker, F. A.; Hodgson, K. O.; Hedman, B.; Solomon, E. I. *Inorg. Chem.* **2009**, *48*, 1678–1688.
- (35) Hocking, R. K.; Debeer George, S.; Raymond, K. N.; Hodgson, K. O.; Hedman, B.; Solomon, E. I. *J. Am. Chem. Soc.* **2010**, *132*, 4006–4015.
- (36) Luo, Y.; Agren, H.; Gel'mukhanov, F. *J. Phys. B: At, Mol. Opt. Phys.* **1994**, *27*, 4169–4180.
- (37) Alexander, J. J.; Gray, H. B. *J. Am. Chem. Soc.* **1968**, *90*, 4260–4271.
- (38) Tanaka, S.; Kotani, A. *J. Phys. Soc. Jpn.* **1993**, *62*, 464–467.
- (39) De Groot, F. *Phys. Rev. B* **1996**, *53*, 7099–7110.
- (40) Shirley, E. L.; Soininen, J.; Zhang, G.; Carlisle, J.; Callcott, T.; Ederer, D.; Terminello, L.; Perera, R. *J. Electron Spectrosc. Relat. Phenom.* **2001**, *114*, 939–946.
- (41) Taguchi, M.; Parlebas, J.; Uozumi, T.; Kotani, A.; Kao, C.-C. *Phys. Rev. B* **2000**, *61*, 2553–2560.
- (42) Josefsson, I.; Kunnus, K.; Schreck, S.; Foehlich, A.; de Groot, F.; Wernet, P.; Odelius, M. *J. Phys. Chem. Lett.* **2012**, *3*, 3565–3570.
- (43) Glatzel, P.; Sikora, M.; Fernandez-Garcia, M. *Eur. Phys. J. Spec. Top.* **2009**, *169*, 207–214.
- (44) Caliebe, W. A.; Kao, C. C.; Hastings, J. B.; Taguchi, M.; Uozumi, T.; de Groot, F. M. F. *Phys. Rev. B* **1998**, *58*, 13452–13458.
- (45) Rueff, J. P.; Journel, L.; Petit, P. E.; Farges, F. *Phys. Rev. B* **2004**, *69*, 235107–(1–9).
- (46) Krisch, M. H.; Sette, F.; Masciovecchio, C.; Verbeni, R. *J. Electron Spectrosc. Relat. Phenom.* **1997**, *86*, 159–164.
- (47) Pirngruber, G. D.; Grunwaldt, J. D.; Roy, P. K.; van Bokhoven, J. A.; Safonova, O.; Glatzel, P. *Catal. Today* **2007**, *126*, 127–134.
- (48) Glatzel, P.; Mirone, A.; Eeckhout, S. G.; Sikora, M.; Giuli, G. *Phys. Rev. B* **2008**, *77*, 115133–(1–7).
- (49) Meyer, D. A.; Zhang, X. N.; Bergmann, U.; Gaffney, K. J. *J. Chem. Phys.* **2010**, *132*, 134502–(1–7).
- (50) George, G. N.; Pickering, I. J. *Exafspak: A Suite of Computer Programs for the Analysis of X-Ray Absorption Spectra*; Stanford Synchrotron Radiation Laboratory: Stanford, CA, 2001.
- (51) Wieghardt, K.; Schmidt, W.; Herrmann, W.; Kuppers, H. *J. Inorg. Chem.* **1983**, *22*, 2953–2956.
- (52) Kotani, A. *J. Synchrotron Radiat.* **2001**, *8*, 110–114.
- (53) Sakurai, J. J., *Advanced Quantum Mechanics*; Addison-Wesley: Reading, MA, 1967.
- (54) Aberg, T. *Phys. Scr.* **1980**, *21*, 495–502.
- (55) De Groot, F.; Krisch, M.; Vogel, J. *Phys. Rev. B* **2002**, *66*, 195112–(1–7).
- (56) Swarbrick, J. C.; Skyllberg, U.; Karlsson, T.; Glatzel, P. *Inorg. Chem.* **2009**, *48*, 10748–10756.
- (57) Glatzel, P.; Weng, T.-C.; Kvashnina, K.; Swarbrick, J.; Sikora, M.; Gallo, E.; Smolentsev, N.; Mori, R. A. *J. Electron Spectrosc. Relat. Phenom.* **2013**, *188*, 17–25.
- (58) DeBeer George, S.; Petrenko, T.; Neese, F. *J. Phys. Chem. A* **2008**, *112*, 12936–12943.
- (59) Chandrasekaran, P.; Stieber, S. C. E.; Collins, T. J.; Que, L., Jr.; Neese, F.; DeBeer, S. *Dalton Trans.* **2011**, *40*, 11070–11079.
- (60) Condon, E. U.; Shortley, G. H. *The Theory of Atomic Spectra*; Cambridge University Press: Cambridge, 1935.
- (61) Cowan, R. D. *The Theory of Atomic Structure and Spectra*; University of California Press: Berkeley, 1981.
- (62) Yamaguchi, T.; Shibuya, S.; Suga, S.; Shin, S. *J. Phys. C: Solid State Phys.* **1982**, *15*, 2641–2650.
- (63) Yamaguchi, T.; Shibuya, S.; Sugano, S. *J. Phys. C: Solid State Phys.* **1982**, *15*, 2625–2639.
- (64) Thole, B. T.; Vanderlaan, G.; Fuggle, J. C.; Sawatzky, G. A.; Karnatak, R. C.; Esteve, J. M. *Phys. Rev. B* **1985**, *32*, 5107–5118.
- (65) De Groot, F.; Fuggle, J.; Thole, B.; Sawatzky, G. *Phys. Rev. B* **1990**, *42*, 5459–5468.
- (66) Ballhausen, C. J. *Introduction to Ligand Field Theory*; McGraw-Hill: New York, 1962.
- (67) Butler, P. H. *Point Group Symmetry Applications: Methods and Tables*; Plenum Press: New York, 1991.
- (68) Tanaka, S.; Okada, K.; Kotani, A. *J. Phys. Soc. Jpn.* **1994**, *63*, 2780–2787.
- (69) Bair, R. A.; Goddard, W. A., III. *Phys. Rev. B* **1980**, *22*, 2767–2776.
- (70) Yamamoto, T. *X-Ray Spectrom.* **2008**, *37*, 572–584.
- (71) DeBeer George, S.; Petrenko, T.; Neese, F. *J. Phys. Chem. A* **2008**, *112*, 12936–12943.
- (72) Vankó, G.; deGroot, F. M. F.; Huotari, S.; Cava, R. J.; Lorenz, T.; Reuther, M. Intersite 4p-3d Hybridization in Cobalt Oxides: A Resonant X-ray Emission Spectroscopy Study. *arXiv:0802.2744v1 [cond-mat.str-el]* [condensed]; **2008**.
- (73) Frisch, M.; et al. *Gaussian 09*, Revision A.02; Gaussian: Wallingford, CT, 2009.
- (74) Tenderholt, A. L. *QMForge*, a program used to analyze the results of quantum chemistry (DFT) calculations, version 2.1, <http://qmforge.sourceforge.net>.
- (75) Hayashi, H.; Kawata, M.; Takeda, R.; Sato, A.; Udagawa, Y.; Kawamura, N.; Nanao, S. *J. Phys. Chem. Solids* **2005**, *66*, 2168–2172.
- (76) Glatzel, P.; Bergmann, U.; de Groot, F. M. F.; Weckhuysen, B. M.; Cramer, S. P. *Phys. Scr.* **2005**, *T115*, 1032–1034.
- (77) Loeffen, P.; Pettifer, R.; Müllender, S.; Van Veenendaal, M.; Röhler, J.; Sivia, D. *Phys. Rev. B* **1996**, *54*, 14877–14880.
- (78) Kroll, T.; Kraus, R.; Schönfelder, R.; Aristov, V. Y.; Molodtsova, O.; Hoffmann, P.; Knupfer, M. *J. Chem. Phys.* **2012**, *137*, 054306–(1–7).
- (79) Bianconi, A.; Dell'Ariceia, M.; Durham, P.; Pendry, J. *Phys. Rev. B* **1982**, *26*, 6502–6508.
- (80) Strange, R.; Alagna, L.; Durham, P.; Hasnain, S. *J. Am. Chem. Soc.* **1990**, *112*, 4265–4268.
- (81) Lancaster, K. M.; Roemelt, M.; Ettenhuber, P.; Hu, Y.; Ribbe, M. W.; Neese, F.; Bergmann, U.; DeBeer, S. *Science* **2011**, *334*, 974–977.
- (82) Pushkar, Y.; Long, X.; Glatzel, P.; Brudvig, G. W.; Dismukes, G. C.; Collins, T. J.; Yachandra, V. K.; Yano, J.; Bergmann, U. *Angew. Chem., Int. Ed.* **2010**, *49*, 800–803.